# A Lightweight and Robust Drone MHz WPT System via Novel Coil Design and Impedance Matching

Yaoxia Shao , *Student Member, IEEE*, Ning Kang, *Student Member, IEEE*, Huan Zhang , *Student Member, IEEE*, Ruihan Ma, *Student Member, IEEE*, Ming Liu , *Senior Member, IEEE*, and Chengbin Ma , *Senior Member, IEEE*

*Abstract*—This article proposes a comprehensive approach to address the challenges posed by the simultaneously varying dc load and coil coupling in drone wireless charging, which inevitably occur during battery charging and landing positioning. The combination of two new coil designs, a quasi-elliptic transmitting (Tx) coil and a "belt" receiving (Rx) coil, enables adequate power transfer at megahertz (e.g., 6.78 MHz) and over a large circular landing area. The on-board "belt" Rx coil (5.8 g) especially helps achieve lightweight and minimize air resistance. A load-pull-based impedance analysis is then performed to clarify the need for an impedance matching network (IMN) on both Rx and Tx sides (i.e., Rx-IMN and Tx-IMN). A new Rx-IMN explicit design is specially developed to significantly limit the range of variation in the coupling coil input impedance, thereby helping to simplify the design of the Tx-IMN to ensure an efficient power amplifier operation. With the proposed coil and IMN designs, actual drone wireless charging experiments demonstrated improved system dc-dc efficiency (max. 83.5%) and dc-dc voltage ratio stability at three representative landing positions (i.e., minimum, medium, and maximum coil coupling).

*Index Terms*—Coil design, drone, impedance matching, megahertz, wireless power transfer.

## I. INTRODUCTION

UNMANNED aerial vehicle (UAV) technology, especially small drones, has grown rapidly in recent years due to advances in onboard sensors (e.g., telephoto cameras, infrared cameras) and battery performance. This makes it possible to deploy drones and their automated stations on a large scale, enabling various applications including line patrol, firefighting, urban security, and environmental monitoring [1], [2]. So far, autonomous drone flight is a mature technology in itself, but there is a lack of low-cost, lightweight solutions for automatic battery charging of drones. Currently, most commercial drone charging stations employ contact charging or battery replacement technology, which has reliability, complexity and cost concerns, especially given the wide variety of outdoor environments [3].

The contactless nature and simplicity of hardware configuration make wireless power transfer (WPT) an attractive and more importantly reliable solution for drone charging stations [4]. Here, two main challenges in implementing WPT are 1) the required small size and light weight of the receiver to minimize the impact on drone aerodynamics, and 2) a sufficiently large charging area because of unavoidable inaccuracy in the landing position [5]. Table I summarizes several representative existing works on drone WPT systems and compares with the proposed system in this article. Note that in the above table, $\eta_{\text{coil}}$ and $\eta_{\text{sys}}$ refer to the coil efficiency and dc-dc system efficiency, respectively. And effective charging areas are normalized by the magnetic flux areas of their respective receiving (Rx) coils, $A_{\text{rx}}$. Among existing works, this article demonstrates the biggest normalized charging area thanks to the megahertz (MHz) operating frequency and compact Rx coil. In [5], a non-uniform spacing coil optimized by a genetic algorithm is proposed to achieve high power transfer efficiency and a large effective charging area, but requires a large Rx coil. Ref. [6] employs a vertical Rx coil to reduce wind resistance and reports a 54.6 g Rx coil with ferrites, but requires push-rods to mechanically align the Rx position. In [7], a sufficiently large charging area can be achieved by replacing the propeller guard with a big Rx coil. This big Rx coil may not be favorable in terms of lightweight and low wind resistance, especially for professional drones. The charging area is dynamically enlarged in [8] by switching between multiple transmitting (Tx) coils according to a specific landing position, but a conventional Rx coil still affects the aerodynamics of the drone. Ref. [9] achieves a constant coil efficiency under a dynamic change of coil coupling through operating frequency modulation. Meanwhile, it does not consider the robustness of the overall system when both the coil coupling and dc load change. In other work targeting drone WPT applications, the requirements for a "large" charging area and a "small" receiver also cannot be met at the same time [10], [11].

For the current application of drone charging stations, it is particularly advantageous to increase the operating frequency of the WPT system to the MHz frequency band, such as at 6.78 MHz [12]. It should be noted that the 6.78 MHz is the lowest frequency in ISM (industrial, scientific, and medical)

TABLE I
EXISTING AND PROPOSED DRONE WIRELESS CHARGING SOLUTIONS

| Coupling Coil Design | Performance |
|---|---|
| | $f = 380$ kHz [5]<br>$P_{\text{out}} = 100$ W<br>$\eta_{\text{coil}} = 92.4\%$<br>Charging area: $4.7 \times A_{\text{rx}}$<br>Rx size: $18 \times 18 \times 5.6$ cm |
| | $f = 85$ kHz [6]<br>$P_{\text{out}} = 87.4$ W<br>$\eta_{\text{sys}} = 87.32\%$<br>Charging area: fixed position<br>Rx size: $13 \times 3.5 \times 0.8$ cm |
| | $f = 13.56$ MHz [7]<br>$P_{\text{out}} = 13$ W<br>$\eta_{\text{sys}} \approx 60\%$<br>Charging area: $1.25 \times A_{\text{rx}}$<br>Rx size: $11 \times 11 \times 0.4$ cm |
| | $f = 302$ kHz [8]<br>$P_{\text{out}} = 183.7$ W<br>$\eta_{\text{coil}} = 90.8\%$<br>Charging area: $5 \times A_{\text{rx}}$ (1 Tx)<br>Rx size: $15 \times 15 \times 0.25$ cm |
| | $f = 0.8–1$ MHz [9]<br>$P_{\text{out}} = 10$ W<br>$\eta_{\text{coil}} = 93.6\%$<br>Charging area: $2.1 \times A_{\text{rx}}$<br>Rx size: $14 \times 14 \times 3$ cm |
| | $f = 6.78$ MHz [this paper]<br>$P_{\text{out}} = 80$ W<br>$\eta_{\text{coil}} = 93.1\%$<br>$\eta_{\text{sys}} = 83.5\%$<br>Charging area: $8.5 \times A_{\text{rx}}$<br>Rx size: $10 \times 2.5 \times 1.7$ cm |

Tx Coil    Rx Coil

bands and the only frequency recommended by ITU-R (International Telecommunication Union Radiocommunication Sector) for consumer MHz WPT applications because of its minimal impact to other licensed bands [13]. MHz operation can effectively reduce the size of coils and circuit components, and improve the spatial freedom of power transfer (i.e., power transfer distance and robustness to coil misalignment) [14]. At the same time, high frequency operation may result in high switching losses. Therefore, topologies with zero-voltage switching (ZVS) and zero-voltage differential switching (ZVDS) properties, such as Class E and Class EF, have been widely used in MHz WPT systems [15], [16], [17], [18]. However, those resonant topologies are known to be sensitive to changes in dc load and coil coupling, which hinder their application in the drone charging. Because the dc load and coil coupling change during battery charging and due

to inaccurate landing position, respectively. Therefore, besides the coil design, many other efforts are required to optimize the topologies and parameters of the circuits when operating at MHz.

In response to the above challenges, this article proposes a systematic approach for a MHz Class $E^2$ WPT system dedicated to drone wireless charging, including new coil and circuit designs. This article has been considerably improved based on its previous conference version [19], including the redesigned Tx coil, explicit design of the Rx impedance matching network (IMN), and new experimental results. The main contributions and organization of this article are briefly explained as follows:

1) Large charging area: A quasi-elliptic Tx coil is proposed to achieve a large circular charging area (Section II-A);
2) Lightweight and compact receiver: A "belt"-inspired Rx coil is designed, which is capable of receiving a sufficient amount of electromagnetic power and weighs only 5.8 g. Compared with the existing coils, this Rx coil enables a low wind resistance and better manufacturing consistency and efficiency (Section II-B).
3) Improving system robustness against simultaneous changes in dc load and coil coupling: An Rx-side impedance matching network (Rx-IMN) and its new explicit design are proposed to minimize the impact of the changing dc load, thereby saving the capacity of the Tx-side impedance matching network (Tx-IMN) to ensure a high-efficiency power amplifier (PA) operation when the relative position of the coupling coils, namely the landing position, changes (Section III).

In addition, the design of Tx-IMN as well as the design of the Class E PA, the sensitivity analysis of the IMNs, and the experimental validation are also provided in the following sections, Sections IV, V, and VI, respectively.

## II. COUPLING COIL DESIGN

For the target application in a drone wireless charging station, the main design purposes of the coupling coils (i.e., Tx and Rx coils) are as follows:

1) The Tx coil should be able to provide sufficiently strong coupling over a wide charging area, due to the inevitable inaccuracy of the landing position.
2) The on-board Rx coil should be as small and as light as possible to minimize its impact on aerodynamics and flight range.
3) The coupling coils should be able to efficiently transfer an expected amount of power within a pre-defined target charging area.

The coupling coils of the proposed drone MHz WPT system are shown in Fig. 1. The quasi-elliptic Tx coil is made of a copper strip, and the Rx coil adopts a "belt"-shaped design and flexible printed circuit (FPC) (hereafter referred to as belt coil). The Rx-IMN and rectifier circuits are housed inside a 3D printed Rx-coil frame to achieve compactness of the receiver (45.6 g in total).
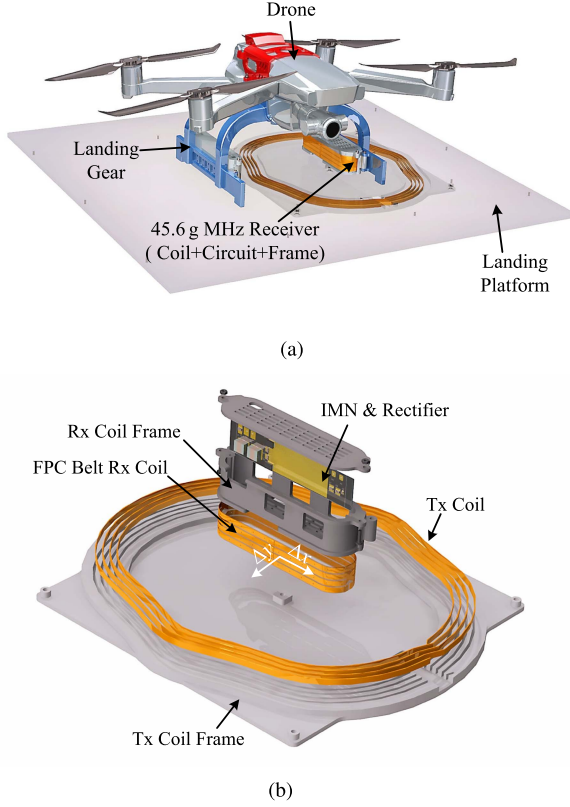
(a)



(b)

Fig. 1. Final design and layout of the proposed drone MHZ WPT system. (a) Overall view. (b) Exploded view.
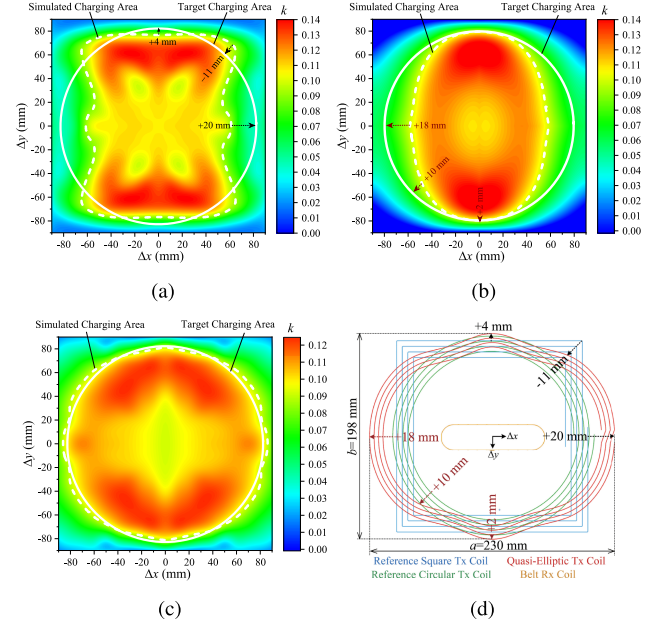


Fig. 2. Design of quasi-elliptic Tx coil based on simulated coupling coefficient distribution of reference Tx coils with basic shapes. (a) Coupling coefficient of a reference square Tx coil. (b) Coupling coefficient of a reference circular Tx coil. (c) Coupling coefficient of the final quasi-elliptic Tx coil. (d) Modification from the reference Tx coils to the quasi-elliptic Tx coil.

## A. Quasi-Elliptic Tx Coil

Considering the randomness of the actual landing position of the drone, the Tx coil should provide a circular area with strong coupling to the Rx coil. It is important to note that this circular "coupling" area does not necessarily correspond to a geometrically circular area due to the specific shape and location of the Rx coil.

After repeating landing tests, the offset radius of a target circular landing zone is determined as 80 mm. Here, the goal of the coil design is defined to achieve a close-to-circular strong "coupling" area that ensures,

$$k \geqslant a_{\mathrm{k}} \cdot k^{\mathrm{max}}, \qquad (1)$$

where $k$ is the coil coupling coefficient and $k^{\mathrm{max}}$ corresponds to the maximum $k$ in the landing zone. $a_{\mathrm{k}}$ is a ratio representing the permissible minimum coil coupling.

Here, a simulation based Tx-coil design is given to modify a reference Tx coil with a basic shape (e.g., square or circular) to a quasi-elliptic Tx coil, which provides a target circular coupling area with an Rx coil of non-circular shape (e.g., the belt Rx coil). Note that $k$ is certainly influenced by the shape, dimension and location of the Rx coil. Thus a geometric square or circular Tx coil can not necessarily guarantee a final coupling area with the same shape. Fig. 2(a) and (b) show the simulation results of the coupling coefficient $k$ between reference Tx coils and the belt Rx coil.

The design procedures of a final Tx coil, such as the above quasi-elliptic Tx coil, are given as follows:
1) The parameter $a_{\mathrm{k}}$ in (1) should be determined as a design guidance. Physically, $a_{\mathrm{k}}$ should be slightly lower than the ratio of $k$ at the center to $k^{\mathrm{max}}$ (about 73% in Fig. 2(a) and (b)) to ensure a continuous charging area. Thus, $a_{\mathrm{k}}$ is taken as 70%. Note that a too small $a_{\mathrm{k}}$ is problematic because it makes the following impedance matching difficult when the coil coupling and dc load vary.
2) The coupling coefficient between a reference Tx coil (square or circular) and the Rx coil is simulated, then the boundary of the relatively strong coupling charging area can be obtained [refer to white dashed lines in Fig. 2(a) and (b), and (1)].
3) The white dashed area is compared with the white target area. The differences (i.e., arrows in Fig. 2(a) and (b)) are used to modify the reference coil to the quasi-elliptic coil. Since the Tx coil design is guided by the differences in the coupling coefficient, the circular shape of the relatively strong coupling charging area is achieved in the final coil design [refer to Fig. 2(c)].

For the MHz WPT (especially for frequency bands above 3 MHz), it is difficult or expensive to fabricate effective Litz wires due to the need of extremely small strand diameters [20], which have been widely used for kHz WPT [21]. Solid copper wire, copper foil and copper tube have been applied to the MHz WPT [22], [23], [24]. Here, Tx coils with different rectangular cross sections are simulated and compared, as shown in Fig. 3. It can be seen that with the same cross-sectional area (red dashed curve), the quality factor of the coil improves more by increasing
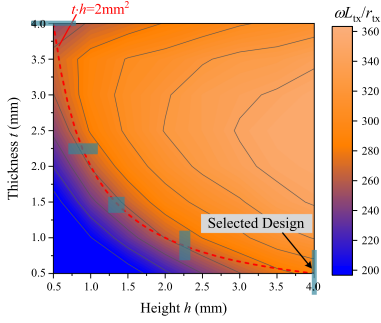
Fig. 3. Quality factor simulation of Tx coils with different cross section sizes.
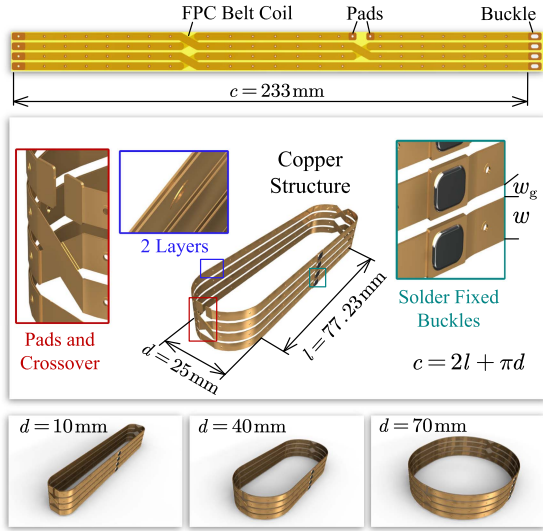


Fig. 4. A deformable Rx belt coil ($N = 4$).

copper height $h$ than by increasing copper thickness $t$. Namely, the strip coil represented by the design at the lower right corner of Fig. 3 is selected. Note that the turn number of the Tx coil should be maximized to achieve an inductance as high as possible but avoid the overvoltage of the compensation capacitor (4 turns here).

### B. Belt Rx Coil

For the MHz WPT, it is possible to use an air-core light PCB (printed circuit board) Rx coil. At present, the majority of the PCB coils are with a planar spiral shape. This conventional planar design is ineffective to pass through a sufficient amount of magnetic flux when a compact Rx coil is required, such as in the current drone application. Therefore, this article proposes a new FPC-based helix belt coil, as shown in Fig. 4. This belt coil is made of a 0.2 mm FPC and weights 5.8 g (2 layers of 2 oz copper foil). A unique "buckle" structure is also proposed to connect the two ends of the FPC coil. It is worthy to mention that the mass production of special-shaped coils is always challenging, but the proposed FPC belt coil is straightforward to fabricate. Fig. 5 shows how the belt coil is formed by soldering "buckles". This
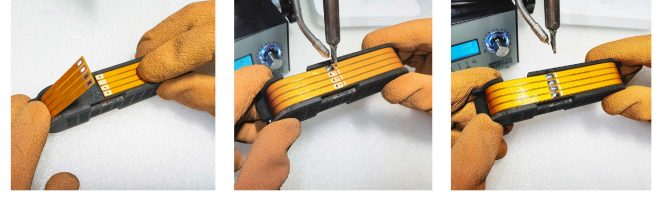


Fig. 5. Forming the belt coil by soldering the "buckles".

coil can also be easily changed to different shapes for various types of drones, namely, i.e., with different $d$'s in Fig. 4 and thus different inductances and quality factors. Note that further reduction in the receiver's weight is possible by replacing the 3D printed frame 21.2 g (46% total weight) with a new design using lighter, stronger materials (such as carbon fiber). The 3D frame used in this article is for rapid-prototyping purposes.

This article also develops an optimal design to analytically optimize the trace width and number of turns of the belt coil, rather than relying on time-consuming finite element analysis (FEA). It is known that the power transfer efficiency improves with

$$\frac{\omega^2 M^2}{r_{tx} r_{rx}}, \tag{2}$$

which relates to the loading effect of the Rx side on the Tx side (i.e., reflected impedance) [14]. Here, $\omega$ is the operating frequency (=6.78 MHz); $M$ is the mutual inductance, and $r_{rx}$ is the ac resistance of the Rx coil. For the present application of the drone wireless charging, the compactness and thus lightweight are very important. Therefore, a new Figure of Merit (FoM) is defined to guide the design of the Rx coil:

$$FoM_{rx} = \frac{M^2}{r_{rx} V_{rx}} = \frac{\Psi_{rx}^2 / I_{tx}^2}{K\,(N_{rx}/w)\,A_{rx}\,[N_{rx} w + (N_{rx} - 1)\,w_g]}, \tag{3}$$

where $V_{rx}$ is the volume of the belt coil; $A_{rx}$ is magnetic flux area of the Rx coil; $I_{tx}$ is the current magnitude in the Tx coil; $N_{rx}$ is the number of turns of the Rx coil; $w$ and $w_g$ are trace width and trace spacing of the Rx coil, respectively [see Fig. 4]; $\Psi_{rx}$ is flux linkage in the Rx coil, and K is a constant related to coil thickness, perimeter and material conductivity.

To calculate $\Psi_{rx}$, for the quasi-elliptic Tx coil, its $z$-direction magnetic induction intensity at the center ($\Delta x = \Delta y = 0$, $k = 73\% k^{max}$) can be approximately calculated by the Biot-Savart law:

$$B_z\,(\Delta z) = \frac{\mu_0 N_{tx} I_{tx} \overline{R}_{tx}^2}{2\left(\overline{R}_{tx}^2 + \Delta z^2\right)^{3/2}}, \tag{4}$$

where $\mu_0$ is vacuum permeability; $N_{tx}$ is the number of turns of the Tx coil; $\Delta z$ is height; and $\overline{R}_{tx}$ is the average radius of the quasi-elliptic Tx coil:

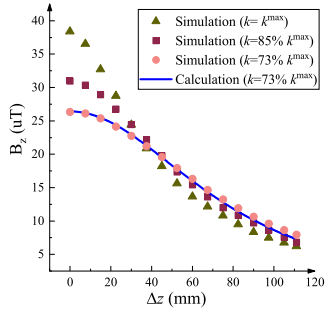$$\overline{R}_{tx} \approx R_{tx}^{max} + R_{tx}^{min}. \tag{5}$$

Fig. 6. Comparison of calculated and HFSS simulated $z$-direction magnetic induction intensities of the quasi-elliptic Tx coil at positions with a different coupling coefficient (note: 73% $k^{\max}$ point locates at the center of the Tx coil).
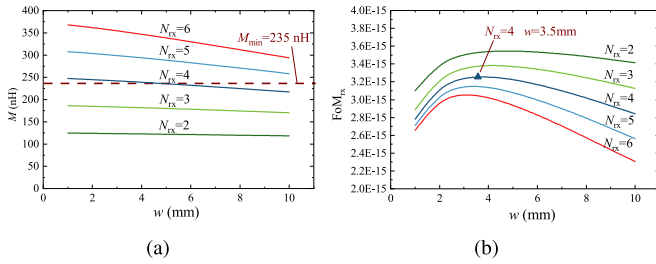


Fig. 7. Graph-aided design of the belt Rx coil ($d$=25 mm, $w_g$=1 mm). (a) $M$ versus $N_{rx}$ and $w$. (b) FoM$_{\mathrm{rx}}$ versus $N_{rx}$ and $w$.
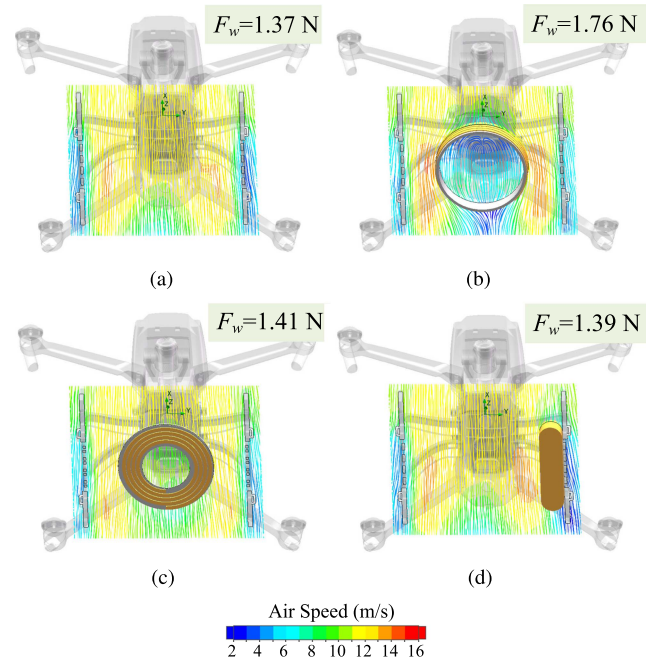


Fig. 8. Simulation of air speed streamlines and wind resistance of Rx coils with different shapes under 40 km/h wind speed. (a) Drone without coil attached. (b) Drone with the helix coil. (c) Drone with the spiral coil. (d) Drone with the belt coil.

The accuracy of (4) is verified by comparing with high-accuracy HFSS simulation results, as shown in Fig. 6. The magnetic induction intensity at the center of the Tx coil (i.e., $k = 73\% k^{\max}$) is weak and thus challenging for the Rx coil design. Therefore, the Rx coil design under $k = 73\% k^{\max}$ is performed to improve the robustness of the wireless charging within the target effective charging area. The flux linkage in the Rx coil can be then approximately obtained as:

$$\Psi_{\mathrm{rx}} = A_{\mathrm{rx}} \sum_{i=1}^{N_{\mathrm{rx}}} B_z \left( \Delta z \right) \big|_{\Delta z = h_{\mathrm{bot}} + 0.5w + (i-1)(w + w_{\mathrm{g}})}, \quad (6)$$

where $h_{\mathrm{bot}}$ is the shortest vertical distance between the Tx coil and the Rx coil. An optimal belt Rx coil can then be designed based on (3). For instance, assuming 1) a 6.78 MHz operating frequency and 2) a target 10 $\Omega$ load impedance of the Rx coil, the minimum mutual inductance $M_{\min}$ is 235 nH to provide a 10 $\Omega$ reflected impedance, which is a reasonable value for the Class E PA operation [see Fig. 9]. Note that the equivalent load of a typical battery changes during charging. Thanks to the following impedance network design in Section III, it is possible to first optimize the Rx coil based on a single nominal Rx-coil load impedance, 10 $\Omega$ here (an average real component of the Rx-coil load impedance without the impedance matching). Through Fig. 7(a) and (b), the optimal design is determined and marked by the blue triangle in Fig. 7(b), by which $M > M_{\min}$, $N_{\mathrm{rx}} = 4$, and $w = 3.5$ mm.

The design procedures of the Tx coil and Rx coil are summarized as follows:

1) Determine the shape and size of the Rx coil based on the shape and size of the drone's landing gear.
2) Achieve an optimal shape (i.e., quasi-elliptic shape here) of the Tx coil based on the modification of a reference coil.
3) Further optimize the number of turns and cross-sectional size of the Tx coil to make its inductance as large as possible, while avoiding the overvoltage of the compensation capacitor, and also reduce the conduction loss.
4) Finalize the optimal design of the Rx coil based on the optimized Tx coil.

The aerodynamic simulation is performed to verify the low wind resistance of the proposed belt Rx coil, as shown in Fig. 8. When wind with a speed of 40 km/h (nominal cruising speed of the selected drone) is applied perpendicular to the front of the drone (i.e., with zero pitch angle), the belt coil has less impact on airflow streamlines than the existing helix coil and spiral coil (with the same outer radius). The increase of wind resistance is 28.8%, 2.9% and 1.4% for the helix coil, spiral coil and belt coil, respectively. Note that the spiral coil further increases the wind resistance when the pitch angle of the drone is not zero.

For the important balance issue, the circuits such as for communication and charging control are placed on the other side of the landing gear. Note that many professional drones have cameras and sensors in the center of the bottom. It is a practical solution to place the receiver and other circuits at the two sides of the landing gear.
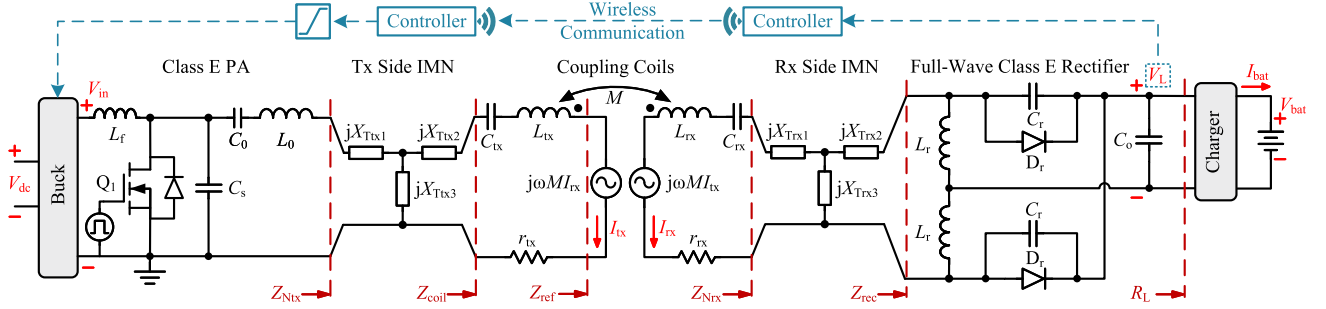
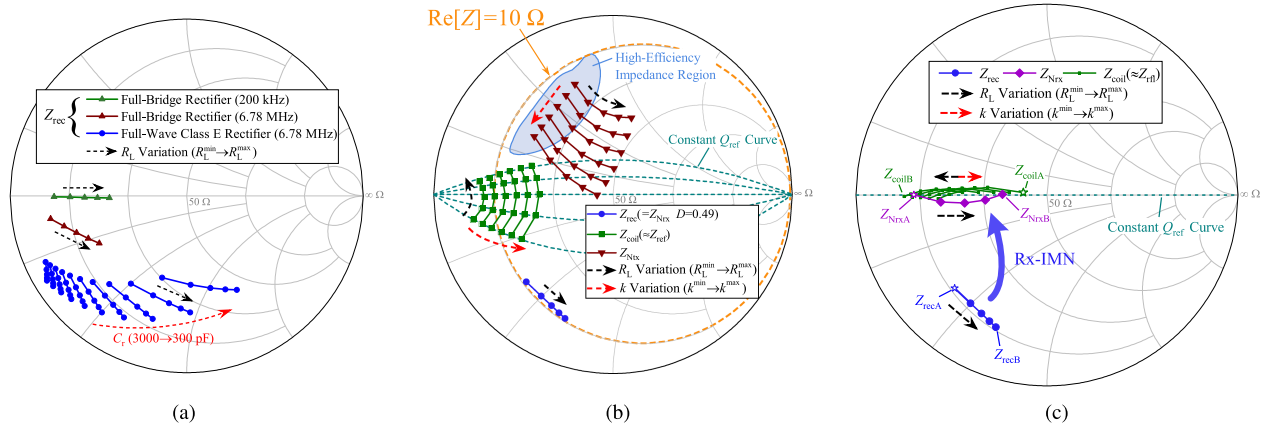Fig. 9. Circuit configuration of a Class $E^2$ drone MHz WPT system.



Fig. 10. Load-pull simulation when both final dc load and coil coupling vary. (a) Input impedance trajectories of the full-bridge rectifier and full-wave Class E rectifier under varying dc load. (b) Impedance trajectories without Rx-IMN. (c) Impedance trajectories with Rx-IMN.

## III. ROBUSTNESS ENHANCEMENT

Fig. 9 shows the circuit configuration of the target drone MHz WPT system. It consists of an input buck converter, a Class E PA, a Tx-IMN, a pair of coupling coils and their two series compensation capacitors, an Rx-IMN, a full-wave Class E rectifier, and an on-board battery charger. In the figure (from right to left), $R_L$ is the equivalent dc input resistance of the battery charger (i.e., the final dc load of the WPT system), $Z_{rec}$ is the rectifier input impedance, $Z_{Nrx}$ is the input impedance of the Rx-IMN, $Z_{ref}$ is the Rx's reflected impedance on the Tx side, $Z_{coil}$ is the input impedance of the coupling coils, and $Z_{Ntx}$ is the input impedance of the Tx-IMN, namely the actual PA load. The input voltage $V_L$ of the battery charger is forwarded as a feedback signal to control the dc supply voltage of the PA, $V_{in}$, in order to maintain a constant $V_L$. Note that in this specific application, the final dc load $R_L$ and mutual inductance of the coupling coils $M$ may considerably vary during the battery charging and at different landing positions, respectively.

### A. Necessity of Matching on Both Rx and Tx Sides

As shown in Fig. 9, $R_L$ is the input resistance of the battery charger, and the input voltage of the charger $V_L$ is constant during the battery charging. Therefore, $R_L$ first slightly drops in the

Constant-Current (CC) mode, and then substantially increases in the Constant-Voltage (CV) mode. Unlike the conventional kHz WPT systems, the MHz WPT systems, such as operating at 6.78 MHz, demonstrate an obvious reactive component of the rectifier input impedance, as shown by the brown and blue curves in Fig. 10(a). This is because of diode parasitics when operating in MHz bands. These reactive impedance trajectories present challenges to the high-efficiency operation of the coupling coils and PA. In Fig. 10(a), the impedance trajectories of the conventional full-bridge rectifier and full-wave Class E rectifier are both shown for reference purposes. Note that the Class E rectifier has an additional degree of design freedom, the capacitances of its two parallel capacitors $C_r$, and these two $C_r$'s are usually determined to be identical to enable a diode duty cycle of $D = 0.49$ at $R_L = R_L^{min}$. This maximizes the rectifier's output capability and avoid diode conduction overlapping.

The variation in $M$, i.e., the relative position of the coupling coils, is an important source of uncertainty due to the drone's landing inaccuracy [see Fig. 9]. Its impact can be described by the reflected impedance $Z_{ref}$. Supposing that $C_{tx}$ fully compensates $L_{tx}$, then the input impedance of the coils $Z_{coil}$ and $Z_{ref}$ are almost equal,

$$Z_{coil} = Z_{ref} + r_{tx} \approx Z_{ref}, \quad (7)$$

where

$$Z_{\text{ref}} = R_{\text{ref}} + jX_{\text{ref}} = \frac{\omega^2 M^2}{Z_{\text{Nrx}} + r_{\text{rx}} + j\left(\omega L_{\text{rx}} - \frac{1}{\omega C_{\text{rx}}}\right)}$$

$$\approx \frac{\omega^2 k^2 L_{\text{tx}} L_{\text{rx}}}{R_{\text{Nrx}} + jX_{\text{Nrx}} + j\left(\omega L_{\text{rx}} - \frac{1}{\omega C_{\text{rx}}}\right)}$$

$$= k^2 \cdot (a + jb) \propto k^2 \left(1 + jQ_{\text{ref}}\right), \tag{8}$$

where $Q_{\text{ref}}$ is the quality factor of the reflected impedance defined by $Q_{\text{ref}} = X_{\text{ref}}/R_{\text{ref}}$. It can be seen from (8) that the coil coupling coefficient has no effect on $Q_{\text{ref}}$. Constant $Q_{\text{ref}}$ curves under a varying $k$ are shown by the dashed cyan curves in the middle of Fig. 10(b).

It has been known that the Tx-IMN is effective to maintain a high efficiency of the PA operation [25]. Meanwhile, when the coil relative position (i.e., $M$) also changes, the Rx-IMN will become necessary. Supposing that there is no Rx-IMN, then $Z_{\text{rec}}$ is simply equal to $Z_{\text{Nrx}}$. The corresponding trajectories of $Z_{\text{coil}}$ are shown by the green curves in the middle of Fig. 10(b) under changing $R_{\text{L}}$ and $k$ [see black and red dashed arrows, respectively]. With the existing Tx-IMN design, those trajectories can be only mapped into the brown trajectories of $Z_{\text{Ntx}}$ (i.e., the actual PA load) in the upper part of Fig. 10(b). The oval-shaped blue shadow illustrates the desired locations of $Z_{\text{Ntx}}$ for an efficient operation of the Class E PA. It is obvious that Tx-IMN alone is incapable to provide the required impedance matching when both the final dc load (i.e., $R_{\text{L}}$) and landing position (i.e., $k$) change. An Rx-IMN is especially needed to suppress the impact of the changing $R_{\text{L}}$, and thus makes it easier for the Tx-IMN to handle the variations in both $k$ (i.e., an uncertain landing position) and $R_{\text{L}}$.

### B. Explicit Design of Rx-IMN

Supposing that $C_{\text{rx}}$ fully compensates $L_{\text{rx}}$, (8) can be rewritten as:

$$Z_{\text{ref}} \approx \frac{\omega^2 M^2}{R_{\text{Nrx}} + jX_{\text{Nrx}}} \propto k^2 \left(R_{\text{Nrx}} - jX_{\text{Nrx}}\right). \tag{9}$$

Thus,

$$Q_{\text{ref}} = \frac{X_{\text{ref}}}{R_{\text{ref}}} = -\frac{X_{\text{Nrx}}}{R_{\text{Nrx}}}. \tag{10}$$

It would be ideal to match the $Z_{\text{ref}}$ trajectory, when $R_{\text{L}}$ changes, to be along one of the constant $Q_{\text{ref}}$ curves, again as shown by the dashed cyan curves in the middle of Fig. 10(b). Thus, the Tx-IMN only needs to match this single curve, when $k$ also changes, into the required high-efficiency region of the PA illustrated by the oval-shaped blue shadow.

The parameters of the Rx-IMN, a T-network, can then be analytically determined as follows. First, the input impedance of the Rx-IMN can be calculated as:

$$Z_{\text{Nrx}} = R_{\text{Nrx}} + jX_{\text{Nrx}} = jX_{\text{Trx1}} + \left(Z_{\text{rec}} + jX_{\text{Trx2}}\right) // jX_{\text{Trx3}}$$

$$= jX_{\text{Trx1}} + \frac{jX_{\text{Trx3}}\left(R_{\text{rec}} + jX_{\text{rec}} + jX_{\text{Trx2}}\right)}{R_{\text{rec}} + jX_{\text{rec}} + jX_{\text{Trx2}} + jX_{\text{Trx3}}}, \tag{11}$$

where $R_{\text{rec}}$ and $X_{\text{rec}}$ are the real component and imaginary component of $Z_{\text{rec}}$; $X_{\text{Trx},i}$'s ($i$=1,2,3) represent reactances of the passive components in the Rx-IMN [see Fig. 9]. Thus, the real component and imaginary component of $Z_{\text{Nrx}}$ can be derived as:

$$\begin{cases} R_{\text{Nrx}} = \text{Re}\left\{Z_{\text{Nrx}}\right\} = \frac{R_{\text{rec}} X_{\text{Trx3}}^2}{\left(X_{\text{Trx2}} + X_{\text{Trx3}} + X_{\text{rec}}\right)^2 + R_{\text{rec}}^2} \\ X_{\text{Nrx}} = \text{Im}\left\{Z_{\text{Nrx}}\right\} \\ = \frac{\left(X_{\text{Trx1}} + X_{\text{Trx3}}\right) R_{\text{rec}}^2 + \left(X_{\text{Trx2}} + X_{\text{Trx3}} + X_{\text{rec}}\right)\left(X_{\text{Trx1}} + X_{\text{Trx3}}\left(X_{\text{Trx2}} + X_{\text{rec}}\right)\right)}{\left(X_{\text{Trx2}} + X_{\text{Trx3}} + X_{\text{rec}}\right)^2 + R_{\text{rec}}^2} \end{cases} \tag{12}$$

In Fig. 10(c), the starting point $Z_{\text{recA}}$ and ending point $Z_{\text{recB}}$ of $Z_{\text{rec}}$ trajectory are shown by the blue curve in the lower part of the figure, corresponding to $R_{\text{L}}^{\text{min}}$ and $R_{\text{L}}^{\text{max}}$, respectively. In order to make the $Z_{\text{Nrx}}$ trajectory as much as possible on a constant $Q_{\text{ref}}$ curve, from (10), one condition is that

$$\frac{X_{\text{NrxA}}}{R_{\text{NrxA}}} = \frac{X_{\text{NrxB}}}{R_{\text{NrxB}}}. \tag{13}$$

The coil efficiency should also be taken into account when designing the Rx-IMN, especially at the maximum output power (i.e., $R_{\text{L}} = R_{\text{L}}^{\text{min}}$). This efficiency can be analytically derived as a function of $k$,

$$\eta_{\text{coil}} = \frac{\omega^2 k^2 L_{\text{tx}} L_{\text{rx}} R_{\text{NrxA}}}{\left(r_{\text{rx}} + R_{\text{NrxA}}\right)\left[\omega^2 k^2 L_{\text{tx}} L_{\text{rx}} + r_{\text{tx}}\left(r_{\text{rx}} + R_{\text{NrxA}}\right)\right]}, \tag{14}$$

assuming $R_{\text{L}} = R_{\text{L}}^{\text{min}}$ thus $Z_{\text{Nrx}} = Z_{\text{NrxA}}$. An average coil efficiency under $R_{\text{L}}^{\text{min}}$ and a varying $k$ can be defined as

$$\overline{\eta}_{\text{coil}} = \frac{\int_{k^{\text{min}}}^{k^{\text{max}}} \eta_{\text{coil}} \cdot dk}{k^{\text{max}} - k^{\text{min}}}, \tag{15}$$

To achieve an optimal $\overline{\eta}_{\text{coil}}$, the target starting point $Z_{\text{NrxA}}^*$ of the input impedance trajectory of the Rx-IMN can be calculated as follows:

$$\begin{cases} R_{\text{NrxA}}^* \Leftarrow \frac{\partial \overline{\eta}_{\text{coil}}}{\partial R_{\text{NrxA}}} = 0 \\ X_{\text{NrxA}}^* = 0 \end{cases} \tag{16}$$

Then, the three parameters of the Rx-IMN can be analytically derived by solving the three independent equations in (13) and (16):

$$\begin{cases} X_{\text{Trx1}} = \frac{\sqrt{2} p_1 p_6 R_{\text{recA}} + p_2 R_{\text{NrxA}}^* - R_{\text{recA}}^2 R_{\text{NrxA}}^*}{2 p_6 R_{\text{recA}}} \\ X_{\text{Trx2}} = \frac{p_4 + p_5 + \sqrt{2} p_1 p_6 - p_6\left(X_{\text{recA}} - X_{\text{recB}}\right)}{2 p_6} \\ X_{\text{Trx3}} = -\frac{p_1}{\sqrt{2}} \end{cases}, \tag{17}$$

where

$$\begin{cases} p_1 = \sqrt{\frac{\left[-p_3 + R_{\text{recA}}^4 + p_2\left(p_6^2 + R_{\text{recB}}^2\right)\right]}{p_6^2 R_{\text{recA}}}} \\ p_2 = p_6^2 + p_4 + R_{\text{recB}}^2 \\ p_3 = R_{\text{recA}}^2\left(p_4 - 2p_6^2 + 2R_{\text{recB}}^2\right) \\ p_4 = \sqrt{\left(p_6^2 + p_7^2\right)\left(p_6^2 + p_8^2\right)} \\ p_5 = -R_{\text{recA}}^2 + R_{\text{recB}}^2 \\ p_6 = X_{\text{recA}} - X_{\text{recB}} \\ p_7 = R_{\text{recA}} + R_{\text{recB}} \\ p_8 = R_{\text{recA}} - R_{\text{recB}}. \end{cases} \tag{18}$$
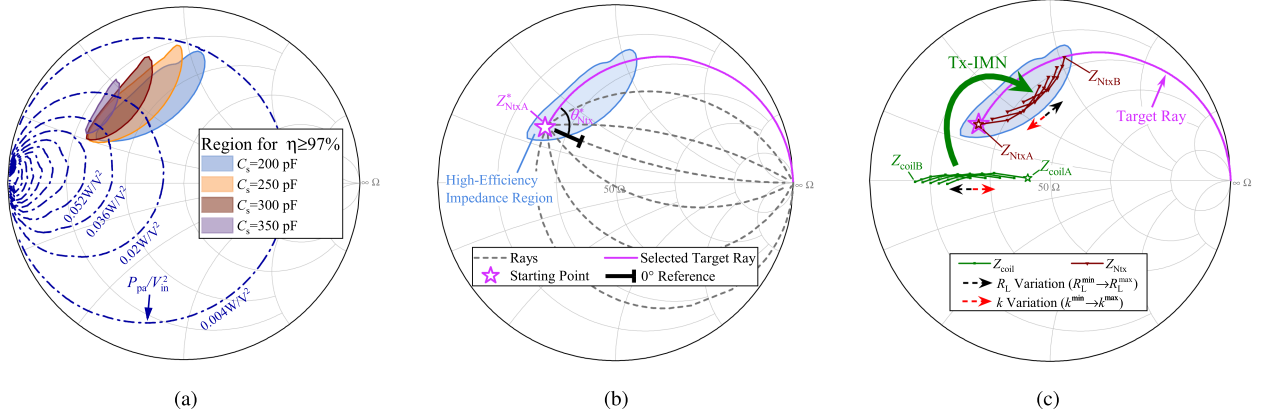
Fig. 11.    Load-pull simulation for PA and Tx-IMN designs. (a) Selection of PA shunt capacitor $C_s$. (b) Selection of a target ray. (c) Tx-IMN design guided by the target ray.

With the above designed Rx-IMN, it becomes possible to match the $Z_{Nrx}$ trajectory into a single curve, the purple curve in Fig. 10(c). This results in a significantly restricted range of variation of the $Z_{coil}$ trajectories (the nearby green curves) compared to their counterparts in Fig. 10(b), which helps alleviate the difficulty of matching the $Z_{Ntx}$ trajectory to the PA high-efficiency region, i.e. the oval-shaped blue shading in Fig. 10(b), by the following Tx-IMN design.

## IV. POWER AMPLIFIER AND TX-IMN DESIGN

The purpose of this section is to optimally design the parameters of PA and Tx-IMN that guarantee a high-efficiency operation of the Class E PA under simultaneously changing dc load and coil coupling (i.e., the uncertainties during battery charging and landing positioning).

### A. Load-Pull-Based PA Design

Fig. 11(a) gives the load-pull simulation results of the Class E PA with different $C_s$, assuming $C_0$ fully compensates $L_0$. In the Smith chart, the contours of the PA's output power (blue dashed curves) and high-efficiency impedance region (oval-shaped color shadows and $\eta_{pa} \geqslant 97\%$) are plotted. It can be seen that a smaller $C_s$ enlarges the PA high-efficiency region. However, $C_s$ should not be too small, otherwise it will reduce the PA's power output capability. In this article, a relatively small $C_s = 220$ pF is chosen to especially enlarge the PA high-efficiency region.

### B. Explicit Design of Tx-IMN

The basic concept of the explicit Tx-IMN design was discussed in Ref. [25]. Note that this existing design cannot handle the simultaneous changes in both dc load and coil coupling that certainly happen in the present application of drone wireless charging. A reference PA load impedance trajectory is first specified as a target ray, which passes through the PA high-efficiency

region (i.e., the oval-shaped blue shadow in Fig. 11(b)) as much as possible. This target ray is then mapped into the purple curve in the upper part of the Smith chart in Fig. 11(b). It is exactly defined by three parameters: 1) real component of $R_{NtxA}^*$, 2) imaginary component of $X_{NtxA}^*$, and 3) angle $\theta_{Ntx}^*$, namely the starting point ($Z_{NtxA}^*$) of the target ray and its direction. The three equations to match the $Z_{Ntx}$ trajectory to the target ray are:

$$Z_{NtxA}^* = Z_{NtxA} \Rightarrow \begin{cases} R_{NtxA}^* = R_{NtxA} \\ X_{NtxA}^* = X_{NtxA} \end{cases}$$

$$\theta_{Ntx}^* = \theta_{Ntx} \Rightarrow \tan(\theta_{Ntx}^*) = \frac{X_{NtxB} - X_{NtxA}}{R_{NtxB} - R_{NtxA}}. \quad (19)$$

The physical meaning of the above three equations are as follows (see Fig. 11(c)):
1) The actual starting point $Z_{NtxA}$ of the Tx-IMN's input impedance trajectory, which corresponds to the case of having $R_L^{min}$ and $k^{max}$ (i.e., with the maximum PA output power), should be positioned at the starting point ($Z_{NtxA}^*$) of the target ray.
2) The ending point $Z_{NtxB}$ should be at another location on the target ray. Note that due to the limited design freedom, only this condition can be theoretically guaranteed.

The analytical solution of (19), i.e., the explicit Tx-IMN parameter design, are in the following form:

$$\begin{cases} X_{Ttx1} = -\frac{(q_1 \pm q_3) R_{NtxA}^*}{2 q_5 R_{coilA}} + \sqrt{\frac{(\pm q_1 q_3 + q_2 q_6) R_{NtxA}^*}{2 q_5^2 R_{coilA}}} + X_{NtxA}^* \\ X_{Ttx2} = \frac{1}{2}\left(\frac{\pm q_1 + q_4}{q_5} + \sqrt{\frac{2(\pm q_1 q_3 + q_2 q_6) R_{NtxA}^*}{q_5^2 R_{coilA}}}\right) - X_{coilB} \\ X_{Ttx3} = -\sqrt{\frac{(\pm q_1 q_3 + q_2 q_6) R_{NtxA}^*}{2 q_3^2 R_{coilA}}} \end{cases}$$

$$\pm : \begin{cases} + & \theta_{Ntx}^* \in (-180°, -90°) \cup (90°, 180°] \\ - & \theta_{Ntx}^* \in (-90°, 90°) \end{cases}, \quad (20)$$
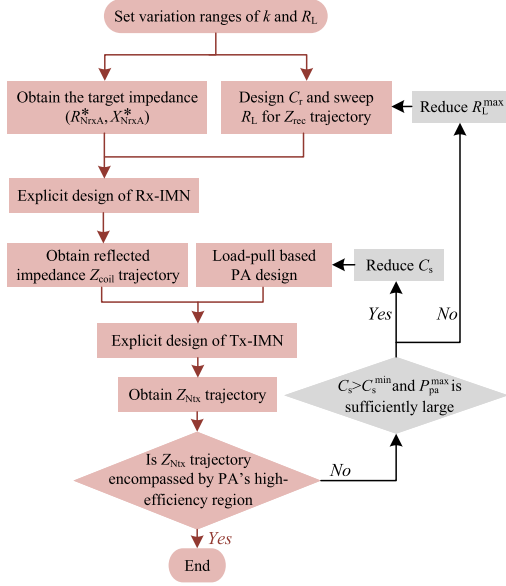
Fig. 12. Parameter design procedure.

where the intermediate variables are calculated as:

$$\begin{cases} q_1 = \sqrt{q_7^2 + q_8^2} \cdot \sqrt{q_8^2 + q_9^2 + 4q_{10}} \\ q_2 = q_8^2 + q_9^2 + 2\left(q_{10} + q_{11}^2 - q_8 q_{11}\right) \\ q_3 = 2q_8 q_{11} - q_8^2 + q_7 q_9 \\ q_4 = 2q_8 q_{12} + q_8^2 + q_7 q_9 \\ q_5 = q_7 \tan\theta_{\text{Ntx}}^* - q_8 \\ q_6 = q_7^2 + q_8^2 \\ q_7 = R_{\text{coilA}} - R_{\text{coilB}} \\ q_8 = X_{\text{coilA}} - X_{\text{coilB}} \\ q_9 = R_{\text{coilA}} + R_{\text{coilB}} \\ q_{10} = R_{\text{coilA}} R_{\text{coilB}} \tan^2\theta_{\text{Ntx}}^* \\ q_{11} = R_{\text{coilA}} \tan\theta_{\text{Ntx}}^* \\ q_{12} = R_{\text{coilB}} \tan\theta_{\text{Ntx}}^* \end{cases} \quad (21)$$

Fig. 12 summarizes the design procedure developed in Sections III and IV. It should be noted that if the changes in coil coupling $k$ and dc load $R_{\text{L}}$ are too large, the $Z_{\text{Ntx}}$ trajectory may exceed the PA's high-efficiency impedance region. In such a case, an iterative process is required to enlarge the high-efficiency impedance region with a smaller $C_s$ or have to reduce the target range of dc load variation [see gray blocks in Fig. 12].

## V. SENSITIVITY ANALYSIS

In the previous sections, explicit designs of Rx-IMN and Tx-IMN were developed. In practical implementations, manufacturing tolerances of passive components (inductors and capacitors) may degrade the matching performance of the IMNs, especially in the MHz bands. This section compares the sensitivity of impedance matching to component tolerances for different IMN topologies and provides practical solutions to mitigate the effect.

T-type IMN and Π-type IMN are equivalent in terms of impedance matching capability, and can be transformed to each
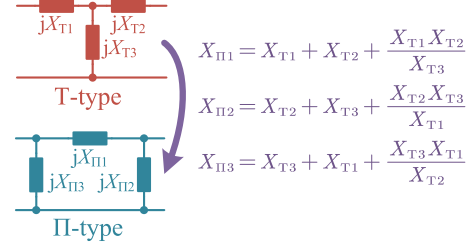


Fig. 13. Transformation from T-type IMN to Π-type IMN.
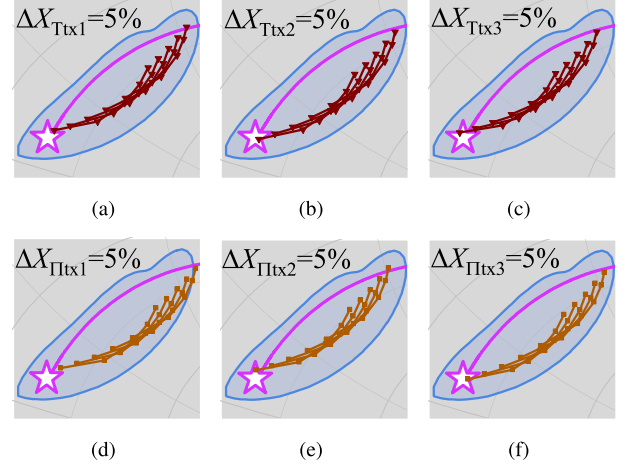


Fig. 14. Effects of parameter tolerances of Tx-IMN on the PA load impedance, $Z_{\text{Ntx}}$. (a)–(c) T-type IMN. (d)–(f) Π-type IMN.

other, as shown in Fig. 13. However, these two IMN topologies are different in terms of parameter sensitivity. Assuming +5% tolerance in the passive components of T-type or Π-type Tx-IMNs ($-5\%$ tolerance has almost an opposite effect), Fig. 14 compares the effect of the above component tolerance to the PA's load impedance $Z_{\text{Ntx}}$. It can be seen that the T-type IMN has low sensitivity to the variations of all its three reactive components, i.e., good robustness. While the Π-type IMN is more sensitive to its upper component $X_{\Pi tx1}$. This component is usually an inductor and naturally has higher manufacturing error than a capacitor. As for the Rx-IMN, T-type IMN still demonstrates low sensitivity to the component tolerance, as shown in Fig. 15. The reflected impedance remains distributed around the constant $Q_{\text{ref}}$ curve with the three component tolerances. However, the Π-type IMN is not suitable for the Rx-IMN implementation because of its high sensitivity to all the three component tolerances.

The number of passive components is another important consideration when implementing the IMNs, since more components lead to higher power loss and larger size. The proposed T-type IMNs are advantageous because half of their passive components can be absorbed both at Tx and Rx sides. In Fig. 16, the actual new components are colored in purple.

The following practical solutions can be used to mitigate the effects of passive component manufacturing tolerances:

TABLE II
RX PARAMETERS OF EXPERIMENTAL SYSTEM

| Different Designs | $L_{rx}$ [nH] | $C'_{rx}$ [pF] $\Rightarrow$ | $X_{Trx1}$ [$\Omega$] | $r_{rx}$ [$\Omega$] | $Q_{rx}$ [$\Omega$] | $L_{Trx2} \Rightarrow$ [nH] | $X_{Trx2}$ [$\Omega$] | $C_{Trx3} \Rightarrow$ [pF] | $X_{Trx3}$ [$\Omega$] | $L_r$ (Choke) [nH] | $C_r$ [pF] | $R_L$ [$\Omega$] |
|---|---|---|---|---|---|---|---|---|---|---|---|---|
| Without Rx-IMN | 1445 | 748 | - | 0.29 | 212 | - | - | - | - | 4.7k | 530 | 7.8–23.4 |
| With Rx-IMN | 1445 | 1160 | 41.3 | 0.29 | 212 | 1990 | 84.7 | 900 | -26.2 | 4.7k | 530 | 7.8–23.4 |

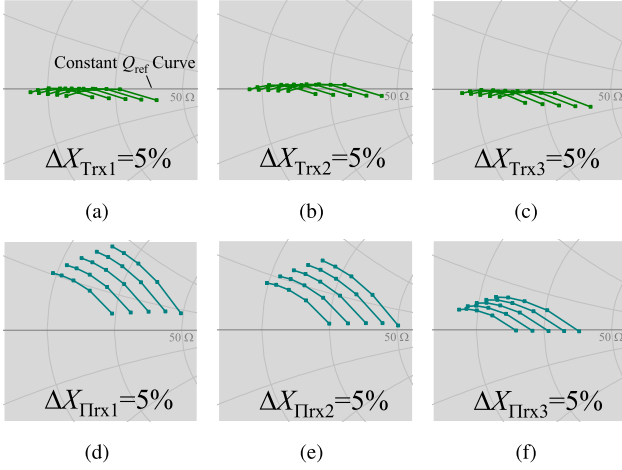

Fig. 15. Effects of parameter tolerances of Rx-IMN on the reflected impedance, $Z_{coil}$. (a)–(c) T-type IMN. (d)–(f) Π-type IMN.
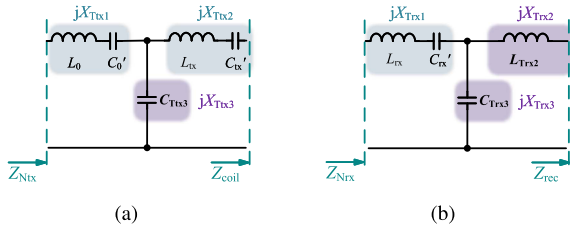


Fig. 16. Implementation of the T-type IMNs (actual new components are colored in purple). (a) Tx-IMN. (b) Rx-IMN.



Fig. 17. Experimental 80-W 6.78-MHz drone wireless charging system and three landing positions. (a) Prototype system. (b) $k = 0.085$. (c) $k = 0.104$. (d) $k = 0.122$.

1) Prioritize the use of T-type IMN, which usually has better robustness over Π-type IMN, and enables absorption of components by the original circuits.
2) Use $L$-$C$ pair instead of a single inductor, through which larger inductor error (e.g. 5%) can be compensated by high-precision capacitors (e.g. 1%).
3) Use measured reflected impedance instead of a simulated one to design the Tx-IMN.

## VI. EXPERIMENTAL VALIDATION

A 80-W 6.78-MHz prototype drone wireless charging system has been built up for validation purposes, as shown in Fig. 17(a). A popular drone, DJI Mavic 2 Enterprise, was chosen as an example target. The Tx PCBs (input buck converter, Class E PA, Tx-IMN, etc.), together with their heat sinks, are mounted above a 3D printed air duct. A 650-V GaN MOSFET GS66504B is used as the PA switch, which is driven by LM5114BMF; PDS3100
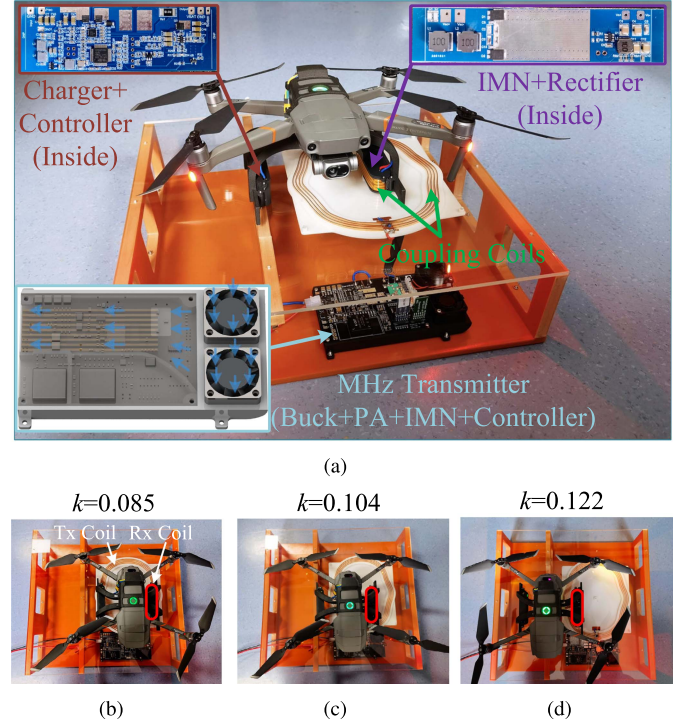
is used as the rectifying diode. The coupling coils designed in Section II ensure that the drone can be effectively charged after landing, as long as the random offset in any direction is within 80 mm. The parameter design (including coils and IMNs) is performed according to the procedures developed in Sections III and IV and listed in Tables II and III. For comparison purposes, the parameters through the conventional design (i.e., without Rx-IMN) are also added. Note that $C'_{rx}$, $C'_0$, and $C'_{tx}$ in the above two tables absorb $X_{Trx1}$, $X_{Ttx1}$, $X_{Ttx2}$, respectively [see Fig. 9]. For the "without Rx-IMN" design in Table II, $C'_{rx}$ is an adjusted final capacitance to compensate the reactive component of the rectifier input impedance [see Section III-A]. Three representative charging positions with minimum (0.085), medium (0.104) and maximum (0.122) coupling coefficients are especially selected in the following experiments [see Fig. 17(b)–(d)].

The experimental $Z_{coil}$ and $Z_{Ntx}$ trajectories in the conventional design are plotted in Fig. 18(a). As same as the discussion at the end of Section III-A, only Tx-IMN cannot prevent the actual $Z_{Ntx}$ (brown curves) from moving away from the PA high-efficiency region. The obvious reactive components in the

TABLE III
Tx PARAMETERS OF EXPERIMENTAL SYSTEM

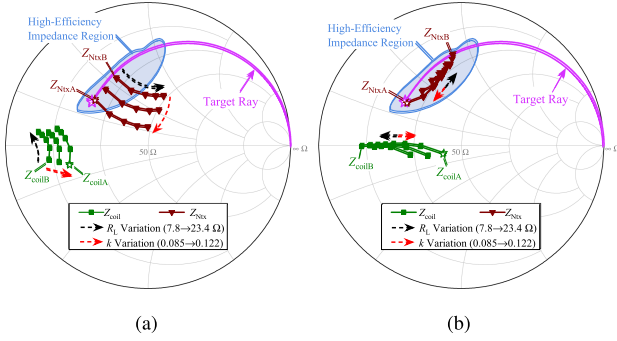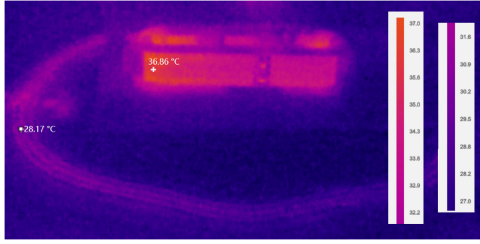| Different Designs | $L_f$ (Choke) [nH] | $C_s$ [pF] | $L_0$ [nH] | $C_0' \Rightarrow$ [pF] | $X_{Ttx1}$ [$\Omega$] | $L_{tx}$ [nH] | $C_{tx}' \Rightarrow$ [pF] | $X_{Ttx2}$ [$\Omega$] | $r_{tx}$ [$\Omega$] | $Q_{tx}$ | $C_{Ttx3} \Rightarrow$ [pF] | $X_{Ttx3}$ [$\Omega$] | $k$ |
|---|---|---|---|---|---|---|---|---|---|---|---|---|---|
| Without Rx-IMN | 10k | 220 | 1975 | 369 | 20.5 | 7100 | 82 | 16.2 | 1.2 | 252 | 804 | -29.2 | 0.085–0.122 |
| With Rx-IMN | 10k | 220 | 1975 | 548 | 41.3 | 7100 | 82 | 16.2 | 1.2 | 252 | 758 | -31.0 | 0.085–0.122 |



Fig. 18. Experimental impedance trajectories of $Z_{coil}$ and $Z_{Ntx}$. (a) Conventional design (i.e., without Rx-IMN). (b) Proposed design.



Fig. 19. Thermal photograph of coupling coils when operating at full power.
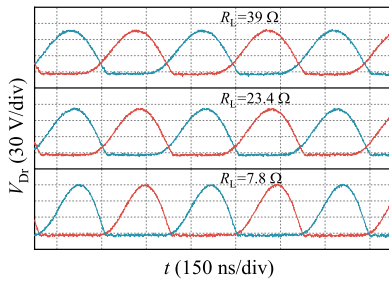


Fig. 20. Voltage waveforms of the full-wave Class E rectifier.

$Z_{coil}$ trajectories (green curves) also indicate that the coupling coils are less efficient. On the contrary, with both Rx-IMN and Tx-IMN (i.e., proposed design), the $Z_{Ntx}$ trajectories (brown curves again) are all well within the PA high-efficiency region [see Fig. 18(b)]. The reactive component of $Z_{coil}$ is also largely suppressed.

Fig. 22 shows the experimental performance of the proposed design (red curves) versus the conventional design (blue curves).
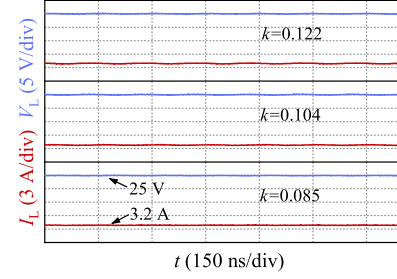


Fig. 21. DC output voltage and current waveforms when operating at full power.

It can be seen that, with the proposed design, both the peak value and stability of the system dc-dc efficiency are significantly improved. The variations of the system efficiency are suppressed from 20% to 9.5%, 22.5% to 6%, and 28% to 6%, respectively, under the three selected landing positions. For example, the peak efficiency is increased from 80% to 83.5% when $k = 0.122$. Another advantage of the proposed design is the more stable dc-dc voltage ratio. In Fig. 22(d)–(f), the proposed design enables an obvious suppression of the variation in $V_{in}$ to keep the battery charger's 25 V input voltage $V_L$, as $R_L$ changes from 7.8 $\Omega$ to 39 $\Omega$ (i.e. from 80 W to 26.7 W), which reduces the loss of the Tx-side buck converter under light loads (i.e., when $R_L$ is large). Due to the minimized number of components when implementing the T-type Tx-IMN and Rx-IMN, these two IMNs consume only 1.37 W additional power at 80 W nominal output power. This level of power loss is worthwhile considering the improved overall system efficiency and robustness.

Fig. 19 shows a thermal steady-state image of the coupling coils at full power. The surface temperatures of the Tx coil and Rx coil are 28.17° C and 36.86° C, respectively, thanks to the large heat dissipation surface of the copper strips.

For reference purposes, the experimental waveforms of the PAs (i.e., the drain-source voltage of the switch $Q_1$) are also given in Fig. 23. The conventional design can only provide ZVS operation when final dc load $R_L = 7.8$ $\Omega$ (i.e., with 80 W maximum output power and $V_L = 25$ V). When the battery charging enters the CV mode, the increased $R_L$ causes the hard-switching and thus a large PA loss and high total harmonic distortion (THD). Again, with the proposed design, the PA can maintain the ZVS operation under all the three different $R_L$. All the experimental results are consistent with the discussions in the above sections, validating the improved robustness of the drone WPT system under realistic scenarios. For reference purposes,

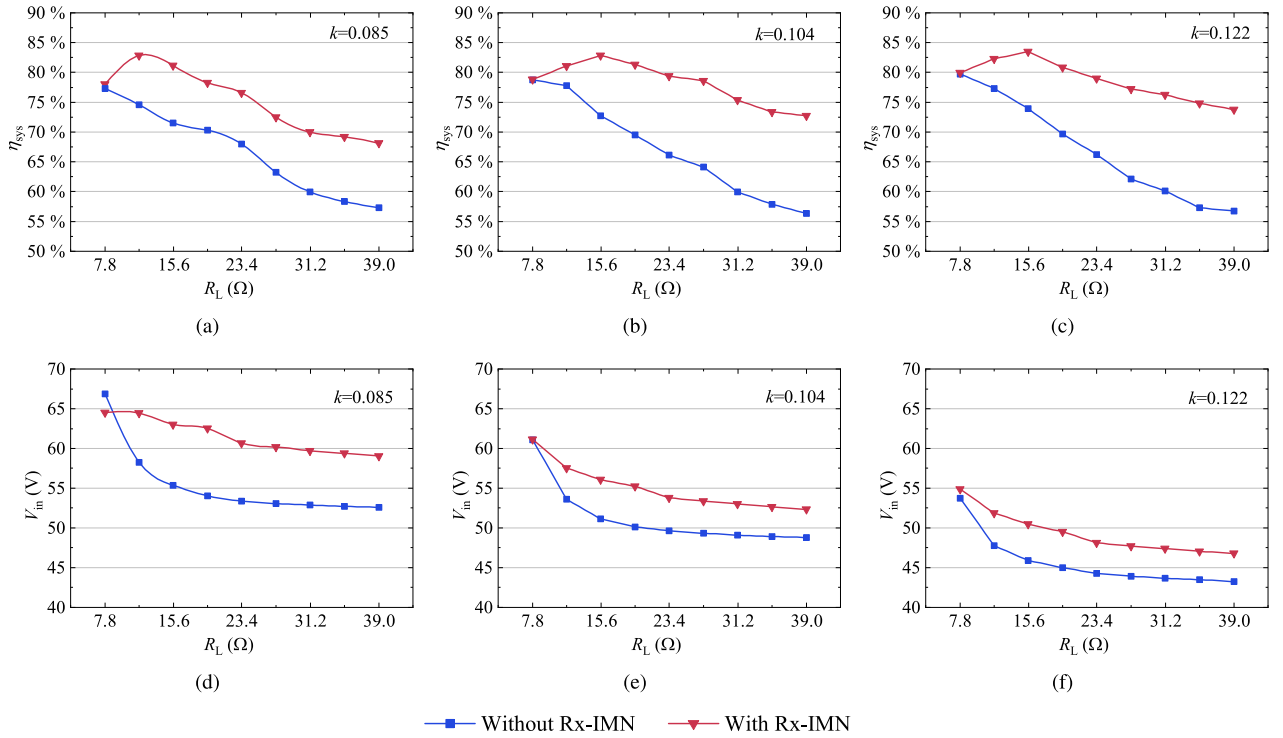Fig. 22. Dc-dc system efficiency $\eta_{sys}$ and required PA input voltage $V_{\text{in}}$ to keep $V_{\text{L}} = 25$ V. (a) $k = 0.085$. (b) $k = 0.104$. (c) $k = 0.122$. (d) $k = 0.085$. (e) $k = 0.104$. (f) $k = 0.122$.
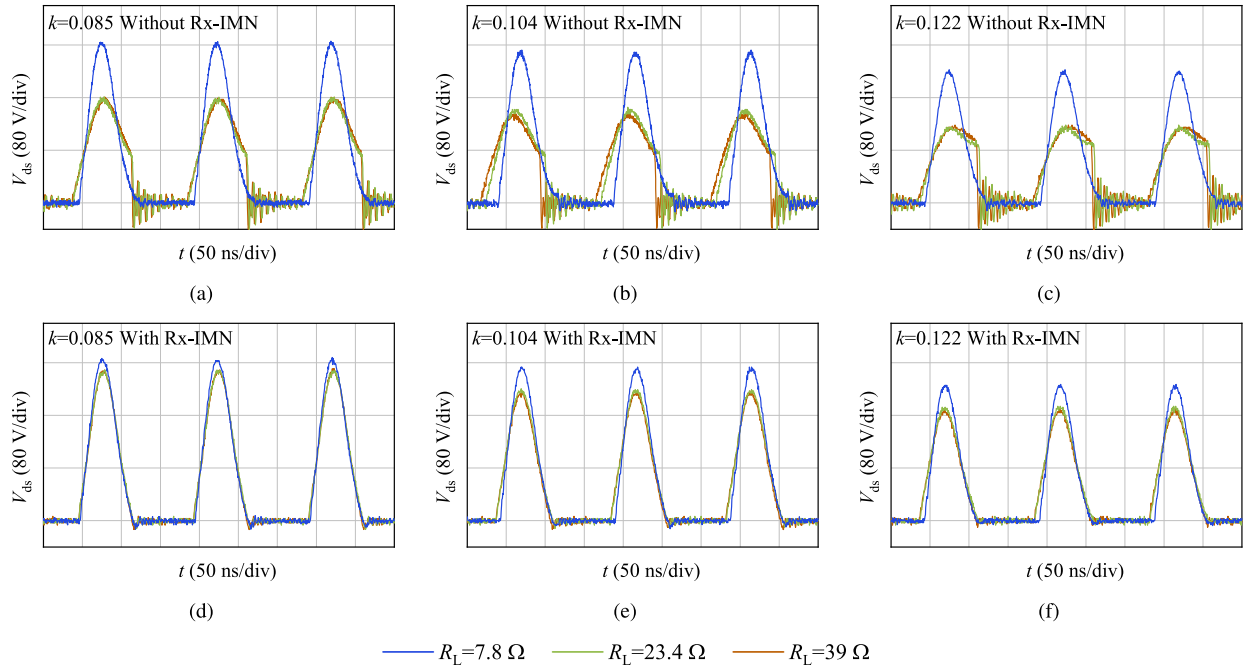


Fig. 23. Drain-source voltage $v_{\text{ds}}$ waveforms of Class E PA. (a) $k = 0.085$. (b) $k = 0.104$. (c) $k = 0.122$. (d) $k = 0.085$. (e) $k = 0.104$. (f) $k = 0.122$.

other voltage and current waveforms are shown in Figs. 20 and 21.

## VII. CONCLUSION

This article presents a systematic and comprehensive approach to address the challenges posed by the simultaneously varying dc load and coil coupling in drone wireless charging. The new coil designs, a quasi-elliptic Tx coil and a "belt" Rx coil, work together to enable adequate wireless transfer of power over a large circular landing area. The "belt" Rx coil especially helps reduce weight and air resistance of the on-board receiver. A load-pull-based impedance analysis is performed to clarify the need for impedance matching on the Rx and Tx sides (i.e. Rx-IMN and Tx-IMN). A new Rx-IMN explicit design is then specially developed to significantly limit the range of variation of the coupling coil input impedance $Z_{\text{coil}}$ compared to the conventional design (i.e., without Rx-IMN). This helps save the capacity of the Tx-IMN to ensure an efficient operation of the PA. Finally, the theoretical analysis and design are validated by the actual drone wireless charging experiments.

## REFERENCES

[1] D. Waleed, S. Mukhopadhyay, U. Tariq, and A. H. El-Hag, "Drone-based ceramic insulators condition monitoring," *IEEE Trans. Instrum. Meas.*, vol. 70, 2021, Art. no. 6007312.

[2] M. Zhang and X. Li, "Drone-enabled Internet-of-Things relay for environmental monitoring in remote areas without public networks," *IEEE Internet Things J.*, vol. 7, no. 8, pp. 7648–7662, Aug. 2020.

[3] D. Lee, J. Zhou, and W. T. Lin, "Autonomous battery swapping system for quadcopter," in *Proc. Int. Conf. Unmanned Aircr. Syst.*, 2015, pp. 118–124.

[4] P. K. Chittoor, B. Chokkalingam, and L. Mihet-Popa, "A review on UAV wireless charging: Fundamentals, applications, charging techniques and standards," *IEEE Access*, vol. 9, pp. 69235–69266, 2021.

[5] C. Rong et al., "Optimization design of resonance coils with high misalignment tolerance for drone wireless charging based on genetic algorithm," *IEEE Trans. Ind. Appl.*, vol. 58, no. 1, pp. 1242–1253, Jan./Feb. 2022.

[6] S. Wu, C. Cai, L. Jiang, J. Li, and S. Yang, "Unmanned aerial vehicle wireless charging system with orthogonal magnetic structure and position correction aid device," *IEEE Trans. Power Electron.*, vol. 36, no. 7, pp. 7564–7575, Jul. 2021.

[7] J. M. Arteaga, S. Aldhaher, G. Kkelis, C. Kwan, D. C. Yates, and P. D. Mitcheson, "Dynamic capabilities of multi-MHz inductive power transfer systems demonstrated with batteryless drones," *IEEE Trans. Power Electron.*, vol. 34, no. 6, pp. 5093–5104, Jun. 2018.

[8] C. Cai, J. Wang, H. Nie, P. Zhang, Z. Lin, and Y.-G. Zhou, "Effective-configuration WPT systems for drones charging area extension featuring quasi-uniform magnetic coupling," *IEEE Trans. Transp. Electrific.*, vol. 6, no. 3, pp. 920–934, Sep. 2020.

[9] J. Zhou, B. Zhang, W. Xiao, D. Qiu, and Y. Chen, "Nonlinear parity-time-symmetric model for constant efficiency wireless power transfer: Application to a drone-in-flight wireless charging platform," *IEEE Trans. Ind. Electron.*, vol. 66, no. 5, pp. 4097–4107, May 2019.

[10] S. A. Al Mahmud, I. Panhwar, and P. Jayathurathnage, "Large-area free-positioning wireless power transfer to movable receivers," *IEEE Trans. Ind. Electron.*, vol. 69, no. 12, pp. 12807–12816, Dec. 2022.

[11] Y. Li, W. Dong, Q. Yang, J. Zhao, L. Liu, and S. Feng, "Mutual-inductance-dynamic-predicted constant current control of LCC-P compensation network for drone wireless in-flight charging," *IEEE Trans. Ind. Electron.*, vol. 69, no. 12, pp. 12710–12719, Dec. 2022.

[12] "A4WP wireless power transfer system baseline system specification (BSS)," Alliance for Wireless Power, Fremont, CA, A4WPS0001 v1.3, Nov. 2014.

[13] "Wireless power transmission using technologies other than radio frequency beam," Radiocommunication Sector of International Telecommunication Union (ITU), Geneva, Switzerland, ITU-R SM.2303-2, Jun. 2017.

[14] M. Liu, H. Zhang, Y. Shao, J. Song, and C. Ma, "High-performance megahertz wireless power transfer: Topologies, modeling, and design," *IEEE Ind. Electron. Mag.*, vol. 15, no. 1, pp. 28–42, Mar. 2021.

[15] N. O. Sokal and A. D. Sokal, "Class E-A new class of high-efficiency tuned single-ended switching power amplifiers," *IEEE J. Solid-State Circuits*, vol. 10, no. 3, pp. 168–176, Jun. 1975.

[16] M. K. Kazimierczuk, "Analysis of class E zero-voltage-switching rectifier," *IEEE Trans. Circuits Syst.*, vol. 37, no. 6, pp. 747–755, Jun. 1990.

[17] J. M. Rivas, Y. Han, O. Leitermann, A. D. Sagneri, and D. J. Perreault, "A high-frequency resonant inverter topology with low-voltage stress," *IEEE Trans. Power Electron.*, vol. 23, no. 4, pp. 1759–1771, Jul. 2008.

[18] X. Zhu, K. Jin, and R. Tan, "Resonant-linear hybrid structure for power amplifier at radio frequency band," *IEEE Trans. Emerg. Sel. Topics Power Electron.*, vol. 9, no. 4, pp. 5113–5124, Aug. 2021.

[19] Y. Shao, R. Ma, H. Zhang, M. Liu, and C. Ma, "Circuit architecture and design of a megahertz wireless power transfer system for drones," in *Proc. Int. Power Electron. Conf.*, 2022, pp. 63–67.

[20] C. R. Sullivan, "High-frequency magnetics design: Overview and winding loss," 2016. [Online]. Available: https://www.psma.com/sites/default/files/uploads/tech-forums-magnetics/presentations/high-frequency-magnetics-design-overview-and-winding-loss.pdf

[21] R. Qin, J. Li, and D. Costinett, "A 6.6-kW high-frequency wireless power transfer system for electric vehicle charging using multilayer nonuniform self-resonant coil at MHz," *IEEE Trans. Power Electron.*, vol. 37, no. 4, pp. 4842–4856, Apr. 2022.

[22] J. Li, R. Qin, J. Sun, and D. Costinett, "Systematic design of a 100-W 6.78-MHz wireless charging station covering multiple devices and a large charging area," *IEEE Trans. Power Electron.*, vol. 37, no. 4, pp. 4877–4889, Apr. 2022.

[23] Z. Tong, W. D. Braun, and J. M. Rivas-Davila, "Design and fabrication of three-dimensional printed air-core transformers for high-frequency power applications," *IEEE Trans. Power Electron.*, vol. 35, no. 8, pp. 8472–8489, Aug. 2020.

[24] S. Aldhaher, D. C. Yates, and P. D. Mitcheson, "Load-independent class E/EF inverters and rectifiers for MHz-switching applications," *IEEE Trans. Power Electron.*, vol. 33, no. 10, pp. 8270–8287, Oct. 2018.

[25] Y. Shao, H. Zhang, M. Liu, and C. Ma, "Explicit design of impedance matching networks for robust MHz WPT systems with different features," *IEEE Trans. Power Electron.*, vol. 37, no. 9, pp. 11382–11393, Sep. 2022.

**Yaoxia Shao** (Student Member, IEEE) received the B.S. degree in mechanical design, manufacturing, and automation, with National Scholarship Honors, from Tongji University, Shanghai, China, in 2018. He is currently working toward the Ph.D. degree in electrical and computer engineering with the University of Michigan-Shanghai Jiao Tong University Joint Institute, Shanghai Jiao Tong University, Shanghai. His research interests include high-frequency power conversion circuits and applications in both inductive power transfer and microwave power transfer. He was the recipient of the Top ten first Stage Proposal Award at the Inaugural IEEE Global Student Wireless Power Competition in 2022, and the Best Paper Award at the IEEE Energy Conversion Congress and Exposition-Asia in 2020.

**Ning Kang** (Student Member, IEEE) received the B.S. degree in information engineering with National Scholarship Honors from the Nanjing University of Aeronautics and Astronautics, Nanjing, China, in 2017. He is currently working toward the Ph.D. degree in electrical and computer engineering with the University of Michigan-Shanghai Jiao Tong University Joint Institute, Shanghai Jiao Tong University, Shanghai, China. His research interests include design and control strategies of megahertz wireless power transfer systems, such as multiple-transmitter systems under FPGA high-speed control.

**Huan Zhang** (Student Member, IEEE) received the B.S. degree in electrical engineering from Shandong University, Jinan, China, in 2016, and the M.S. degree in electrical engineering from Shanghai Jiao Tong University, Shanghai, China, in 2019. He is currently working toward the Ph.D. degree in electrical and computer engineering with the University of Michigan-Shanghai Jiao Tong University Joint Institute, Shanghai Jiao Tong University. His research interests include high-frequency power electronics and its applications in megahertz wireless power transfer and energy routers. Mr. Zhang was the recipient of the Top ten first Stage Proposal Award at the Inaugural IEEE Global Student Wireless Power Competition in 2022, and the Best Paper Award at the IEEE Energy Conversion Congress and Exposition-Asia in 2020.

**Ruihan Ma** (Student Member, IEEE) received the B.S. degree in information engineering with National Scholarship Honors from South China University of Technology, Guangzhou, China, in 2021. He is currently working toward the Ph.D. degree in electrical and computer engineering with the University of Michigan-Shanghai Jiao Tong University Joint Institute, Shanghai Jiao Tong University, Shanghai, China. His research interests include design and control strategies of kilohertz wireless power transfer systems, such as systems with multiple transmitters and receivers.

**Ming Liu** (Senior Member, IEEE) received the B.S. degree in mechatronic engineering from Sichuan University, Sichuan, China, in 2007, and the Ph.D. degree in electrical and computer engineering from the University of Michigan-Shanghai Jiao Tong University Joint Institute, Shanghai Jiao Tong University, Shanghai, China, in 2017. From 2017 to 2020, he was a Postdoctoral Research Fellow at the Department of Electrical Engineering, Princeton University, Princeton, NJ, USA. He joined the School of Electronic Information and Electrical Engineering, Shanghai Jiao Tong University, in 2020, where he is currently an Associate Professor of electrical engineering. His research interests include megahertz wireless power transfer, battery management systems, high frequency high performance power electronics for emerging applications. Dr. Liu was the recipient of Top Ten Academic Star Award and Excellent Ph.D. Thesis Award Nomination from Shanghai Jiao Tong University in 2016 and 2018, Research Excellence Award from AirFuel Alliance, USA, in 2019, and Best Paper Award of IEEE ECCE-Asia in 2020. He was the Guest Editor of IEEE TRANSACTIONS ON INDUSTRIAL INFORMATICS and is the Chair of the Wireless Power Transfer for Energy Storage Charging Subcommittee of Energy Storage Technical Committee, IEEE Industrial Electronics Society.

**Chengbin Ma** (Senior Member, IEEE) received the B.S. degree in industrial automation from the East China University of Science and Technology, Shanghai, China, in 1997, and the M.S. and Ph.D. degrees in electrical engineering from The University of Tokyo, Tokyo, Japan, in 2001 and 2004, respectively. From 2004 to 2006, he was an R&D Researcher with Servo Motor Laboratory, FANUC Limited, Japan. Between 2006 and 2008, he was a Postdoctoral Researcher at the Department of Mechanical and Aeronautical Engineering, University of California, Davis, CA, USA. In 2008, he joined the University of Michigan-Shanghai Jiao Tong University Joint Institute, Shanghai Jiao Tong University, Shanghai, China, where he is currently an Associate Professor of electrical and computer engineering. His research interests include battery and energy management, wireless power transfer, dynamics and motion control, and wide applications in electronic devices, electric vehicles, microgrids, smart grids. Dr. Ma was the recipient of many teaching and research awards at Shanghai Jiao Tong University, such as Teaching and Education Award in 2020 and Koguan Top Ten Research Group Award in 2014. He also was the recipient of the Research Excellence Award from AirFuel Alliance, USA, in 2019. He is an Associated Editor for IEEE TRANSACTIONS ON INDUSTRIAL INFORMATICS and IEEE JOURNAL OF EMERGING AND SELECTED TOPICS IN INDUSTRIAL ELECTRONICS. He served as Delegate of Energy Cluster and is currently the Chair of Shanghai Chapter, IEEE Industrial Electronics Society.